A natural mutation between SARS-CoV-2 and SARS-CoV determines neutralization by a cross-reactive antibody

Nicholas C. Wu[1,2,*], Meng Yuan[3,*], Sandhya Bangaru[3,*], Deli Huang[4,*], Xueyong Zhu[3], Chang-Chun D. Lee[3], Hannah L. Turner[3], Linghang Peng[4], Linlin Yang[4], David Nemazee[4], Andrew B. Ward[3,§], Ian A. Wilson[3,5,§]

[1] Department of Biochemistry, University of Illinois at Urbana-Champaign, Urbana, IL 61801, USA

[2] Carl R. Woese Institute for Genomic Biology, University of Illinois at Urbana-Champaign, Urbana, IL 61801, USA

[3] Department of Integrative Structural and Computational Biology, The Scripps Research Institute, La Jolla, CA 92037, USA

[4] Department of Immunology and Microbiology, The Scripps Research Institute, La Jolla, CA 92037, USA

[5] The Skaggs Institute for Chemical Biology, The Scripps Research Institute, La Jolla, CA, 92037, USA

* These authors contributed equally to this work

§ Correspondence: andrew@scripps.edu (A.B.W.) and wilson@scripps.edu (I.A.W.)

ABSTRACT

Epitopes that are conserved among SARS-like coronaviruses are attractive targets for design of cross-reactive vaccines and therapeutics. CR3022 is a SARS-CoV neutralizing antibody to a highly conserved epitope on the receptor binding domain (RBD) on the spike protein that can cross-react with SARS-CoV-2, but with lower affinity. Using x-ray crystallography, mutagenesis, and binding experiments, we illustrate that of four amino acid differences in the CR3022 epitope between SARS-CoV-2 and SARS-CoV, a single mutation P384A fully determines the affinity difference. CR3022 does not neutralize SARS-CoV-2, but the increased affinity to SARS-CoV-2 P384A mutant now enables neutralization with a similar potency to SARS-CoV. We further investigated CR3022 interaction with the SARS-CoV spike protein by negative-stain EM and cryo-EM. Three CR3022 Fabs bind per trimer with the RBD observed in different up-conformations due to considerable flexibility of the RBD. In one of these conformations, quaternary interactions are made by CR3022 to the N-terminal domain (NTD) of an adjacent subunit. Overall, this study provides insights into antigenic variation and potential for cross-neutralizing epitopes on SARS-like viruses.

INTRODUCTION

The ongoing COVID-19 pandemic, which is caused by the new coronavirus SARS-CoV-2, continues to escalate. Investigating the immunogenicity and antigenicity of SARS-CoV-2 is of great importance for vaccine and therapeutic development. The major antigen of coronavirus is the spike (S) glycoprotein, which is expressed as a homotrimer on the virus surface. Since the S protein is essential for virus entry through engaging the host receptor and mediating virus-host membrane fusion, many antibodies to the S protein are neutralizing [1-12]. The S proteins of SARS-CoV-2 and SARS-CoV, which caused a global outbreak in 2003, have an amino-acid sequence identity of around 77% [13] that leads to differences in antigenicity in serology studies [14, 15]. Although a few monoclonal antibodies have been discovered that can cross-neutralize SARS-CoV and SARS-CoV-2 [6, 7, 16, 17], they seem to be relatively rare in COVID-19 patients [1, 3, 4, 14]. Thus, the molecular determinants that define the antigenic differences and similarities between SARS-CoV-2 and SARS-CoV need further exploration.

CR3022 was previously isolated from a SARS survivor and neutralizes SARS-CoV [18], CR3022 was recently found to also be a cross-reactive antibody that can bind to both SARS-CoV-2 and SARS-CoV [19]. Our recent crystal structure demonstrated that CR3022 targets a highly conserved cryptic epitope on the receptor binding domain (RBD) of the S protein [20]. The CR3022 epitope is exposed only when the RBD is in the “up” but not the “down” conformation on the S protein [20]. A few SARS-CoV-2 antibodies from COVID-19 patients have also recently been shown to target the CR3022 epitope [12, 17, 21], suggesting that it is an important site of vulnerability for the antibody response in SARS-CoV-2 infection. Out of 28 residues in the CR3022 epitope, 24 are conserved between SARS-CoV-2 and SARS-CoV, explaining the cross-reactive binding of CR3022. However, CR3022 has a higher affinity to SARS-CoV than to SARS-CoV-2 (>100-fold difference),

and can neutralize SARS-CoV, but not SARS-CoV-2, in a live virus neutralization assay [20]. Therefore, CR3022 provides a good case study to probe antigenic variation between SARS-CoV-2 and SARS-CoV.

We therefore aimed to dissect the molecular basis underlying the difference in binding affinity and neutralization potency of CR3022 to SARS-CoV-2 and SARS-CoV. The crystal structure of SARS-CoV RBD in complex with CR3022 was determined to compare with the corresponding SARS-CoV-2 RBD structure [20]. In combination of mutagenesis and binding experiments, we demonstrate that a single amino-acid difference at residue 384 (SARS-CoV-2 numbering) between the RBDs of SARS-CoV-2 and SARS-CoV can fully explain the affinity difference with CR3022. Moreover, CR3022 is now able to neutralize SARS-CoV-2 P384A with a similar potency to SARS-CoV. We further investigated the molecular recognition of CR3022 to the SARS-CoV-2 spike protein by electron microscopy and found that rotational flexibility of the RBD resulted in antibody binding to different variants of up-conformations of the RBD relative to the spike trimer. Our findings validate the CR3022 epitope as an important site of vulnerability for a cross-neutralizing antibody response. Throughout this study, residues on RBD are numbered according to SARS-CoV-2 numbering unless otherwise stated.

RESULTS

P384A increases binding affinity of SARS-CoV-2 RBD to CR3022

The epitope of CR3022 in SARS-CoV-2 and SARS-CoV differs by four residues. We aimed to determine whether amino-acid variants in these four non-conserved residues influence the binding affinity of CR3022 to RBD. Four SARS-CoV-2 RBD mutants, namely A372T, P384A, T430M, and H519N (SARS-CoV-2 numbering), were recombinantly expressed and examined (Figure 1A). These mutants converted the amino-acid sequence

of the CR3022 epitope in the SARS-CoV-2 RBD to that of SARS-CoV at each of the four non-conserved residues. While binding of CR3022 mutants A372T (K_D = 66 nM), T430M (K_D = 64 nM), and H519N (K_D = 60 nM) was comparable to wild type (WT) SARS-CoV-2 RBD (K_D = 68 nM), binding of CR3022 to the P384A mutant (K_D = 1.4 nM) was greatly increased (Figure 1B), akin now to that with the SARS-CoV RBD (K_D = 1.0 nM) [20]. Thus, the difference in binding affinity of CR3022 to SARS-CoV-2 RBD versus SARS-CoV RBD can be attributed due to a single amino-acid difference at residue 384.

CR3022 neutralizes SARS-CoV-2 P384A but not WT

While CR3022 can neutralize SARS-CoV [18, 20], multiple groups have shown that it does not neutralize SARS-CoV-2 [3, 5, 20, 22]. One possibility is that the affinity of CR3022 to SARS-CoV-2 RBD is not sufficient to confer neutralizing activity. To test this hypothesis, we compared neutralization of SARS-CoV-2 WT and the P384A mutant by CR3022. Consistent with previous studies [3, 5, 20, 22], CR3022 failed to neutralize SARS-CoV-2 WT (Figure 2). However, CR3022 is now able to neutralize the SARS-CoV-2 P384A mutant at an IC_{50} of 3.2 μg/ml, which is comparable to its neutralizing activity to SARS-CoV (IC_{50} of 5.2 μg/ml). This finding validates the CR3022 epitope as a neutralizing epitope in both SARS-CoV-2 and SARS-CoV, provided that the antibody affinity can surpass a threshold for detection of neutralization.

Previous studies have indicated IgG bivalent binding can play an important role in mediating neutralization of SARS-CoV-2, since the neutralization potency for many antibodies is much greater when expressed as IgG rather than Fab [21, 23]. Subsequently, we also tested the neutralizing activity of CR3022 Fab. Interestingly, the CR3022 Fab neutralized SARS-CoV-2 P384A mutant with an IC_{50} of 4.4 μg/ml, which is similar to that of CR3022 IgG (3.2 μg/ml) (Figure 2). This result indicates that CR3022, unlike many other

SARS-CoV-2 antibodies [21, 23], does not act bivalently with the S proteins on the virus surface and, hence, neutralization is more sensitive to Fab binding affinity.

Sequence conservation of residue 384

We then examined the sequence conservation of residue 384 in other SARS-related coronaviruses (SARSr-CoV) strains. Most SARSr-CoV strains have Pro at residue 384, as in SARS-CoV-2. Only those strains that are phylogenetically very close to SARS-CoV, such as bat SARSr-CoV WIV1 and bat SARSr-CoV WIV16, have Ala at residue 384 (Figure 3A). Phylogenetic analysis implies that P384A emerged during the evolution of SARSr-CoV in bats (Figure 3A), which is the natural reservoir of SARSr-CoV [24]. However, it is unclear whether the emergence of P384A is due to neutral drift or positive selection in bats or other species. In addition, given that residue 384 is proximal to the S2 domain when the RBD is in the “down” conformation (Figure 3B), whether P384A can modulate the conformational dynamics of the “up and down” configurations of the RBD in the S trimer and influence the viral replication fitness will require additional studies.

Crystal structure reveals the impact of P384A in CR3022 binding

We further determined the x-ray structure of SARS-CoV RBD in complex with CR3022 to 2.7 Å resolution (Figure 4A, Supplementary Table 1, and Supplementary Figure 1). The overall structure of CR3022 in complex with SARS-CoV RBD is similar to that with SARS-CoV-2 RBD [20] (Cα RMSD of 0.5 Å for 343 residues in the RBD and Fab variable domain, cf. fig. S2A and B of [20]) (Supplementary Figure 2). Nonetheless, the CR3022 elbow angles, which are distant from the antibody-antigen interface, differ in the two structures, as we mutated the elbow region (as described in [25]) of CR3022 to promote crystallization with SARS-CoV RBD. The conserved binding mode of CR3022 to SARS-CoV-2 RBD and

143 SARS-CoV RBD indicates that the difference in binding affinity of CR3022 between SARS-
144 CoV-2 RBD and SARS-CoV RBD is only due to a very subtle structural difference.
145
146 To investigate how P384 and A384 lead to differential binding of CR3022, we compared
147 the RBD structures from SARS-CoV and SAR-CoV-2 when bound with CR3022. The
148 RBDs have a Cα RMSD of only 0.6 Å (0.7 Å for CR3022 epitope residues). At residue
149 384, the backbone of SARS-CoV-2 is further from CR3022, as compared to that of SARS-
150 CoV (Figure 4B). This difference in backbone positioning (~1.3 Å shift) affects the
151 interaction of the RBD with CR3022 V_H S96, which is encoded by IGHD3-10 gene segment
152 on CDR H3 [18, 20]. While CR3022 V_H S96 forms a hydrogen bond (H-bond) with the
153 T385 side chain in both SARS-CoV-2 RBD and SARS-CoV RBD, it can form a second H-
154 bond with the backbone amide of T385 in SARS-CoV RBD (Figure 4C), but not SARS-
155 CoV-2 RBD (Figure 4D). In addition, CR3022 V_H S96 adopts different side-chain rotamers
156 when binding to SARS-CoV-2 and to SARS-CoV. Consequently, V_H S96 can make an
157 intramolecular H-bond with V_H T31 when CR3022 binds to SARS-CoV RBD (Figure 4C),
158 but not to SARS-CoV-2 (Figure 4D). In summary, V_H S96 forms three H-bonds when
159 CR3022 binds to SARS-CoV RBD, as compared to only one when CR3022 binds to
160 SARS-CoV-2 RBD. This observation indicates why binding of CR3022 to the SARS-CoV
161 RBD is energetically more favorable than to the SARS-CoV-2 RBD.
162
163 **CR3022-bound SARS-CoV S protein exhibits a rare three-up conformation**
164 To understand the binding of CR3022 to the RBD in the context of the homotrimeric S
165 protein, we previously proposed a structural model where CR3022 could only access its
166 epitope on the S protein when at least two RBD are in the “up” conformation and the RBD
167 is rotated relative to its unliganded structure [20]. To further evaluate and expand on this
168 model, negative-stain electron microscopy (nsEM) was performed on CR3022 in complex

with a stabilized version of the SARS-CoV homotrimeric S protein (Figure 5A, see Materials and Methods). The 3D nsEM reconstruction revealed that one SARS-CoV S protein could simultaneously bind to three CR3022 Fabs, with all three RBDs in the "up" conformation (Figure 5B). Consistent with the structural model that we previously proposed [20], the CR3022-bound RBD was indeed rotated compared to that in the unliganded S protein [26-28], such that, in this conformation, steric hinderance between CR3022 and the N-terminal domain (NTD) is minimized.

While our results here demonstrate that CR3022 Fab could form a stable complex with SARS-CoV S protein in a prefusion conformation, a recent study reported that prefusion SARS-CoV-2 S protein fell apart upon binding to CR3022 Fab as indicated by cryo-EM [29]. It should be noted that the three-up conformation is much more rarely observed than the other RBD conformations (all-down, one-up, and two-up) in SARS-CoV by cryo-EM [26-28], or SARS-CoV-2 by cryo-EM [30-32] and cryo-electron tomography [33, 34], and could relate to differences in the stability of S trimers in SARS-CoV versus SARS CoV-2 when CR3022 is bound. Further studies will be required to investigate whether such a difference between SARS-CoV-2 and SARS-CoV is related to stability differences in the recombinant spike proteins, or to different dynamics of the RBD on the virus or infected cells.

RBD flexibility and quaternary interactions in CR3022-bound SARS-CoV S protein

To address some of these issues, we performed cryo-EM analysis to interrogate the binding of CR3022 to SARS-CoV S protein at higher resolution (Supplementary Figure 3 and Supplementary Table 2). Focused 3D classification yielded 4 different structural classes with classes 2 and 4 being nearly identical at the given resolution (Figure 5C and Supplementary Figure 4). Class 3 is the most similar to the model from nsEM, although

the total particle number for classes 2 and 4 together exceed that for class 3 (Supplementary Figure 4). In contrast, class 1 is the least represented. In classes 2 and 4, CR3022 also appears to make quaternary contacts with the NTD, as suggested by well-defined density in the CR3022-NTD interface (Figure 5C). The moderate resolution (6 to 7 Å) of the reconstructions precludes atomic-level descriptions, but the framework region of the CR3022 light chain in classes 2 and 4 is in close proximity to a loop region in NTD corresponding to residues 106-110. In addition, the constant region of CR3022 appears to contact residue D23 of NTD. Another important observation is that the Fab in class 2 and 4 would clash with the adjacent RBD if it were in the "down" conformation. So, for the Fab to exist in this quaternary conformation, the adjacent RBD has to be in the "up" conformation. To evaluate the different dispositions of the RBD in these structures, we compared the cryo-EM structure of an apo form of the SARS-CoV S protein where one RBD is the "up" conformation (PDB 6ACD) [35]. The RBD in classes 1 to 4 are rotated by 84.1°, 54.3°, -54.7°, and 53.7°, respectively, relative to the apo one-up conformation (see Materials and Methods). Furthermore, the CR3022-bound RBD in class 2 and 4 is more open than in the apo form (Supplementary Figure 5), demonstrating the rotational flexibility of the RBD. In fact, RBD conformational flexibility has also been noted in an ACE2-bound SARS-CoV S protein. Three different dispositions (1 to 3) of the RBD were observed in ACE2-bound SARS-CoV S protein with RBD tilts relative to horizontal top surface of the S trimer of 51.2°, 73.3° and 111.6° compared to 68.9° for the apo one-up structure [35]. Our classes 2 and 4 appear to be somewhat intermediate between dispositions 2 and 3 (Supplementary Figure 6), whereas the other classes differ from the RBD dispositions in the ACE2-bound SARS-CoV S structures. However, despite the flexibility of CR3022-bound RBD, bivalent binding of CR3022 to S protein does not seem to occur on the virus surface since an IgG avidity effect was not observed in the neutralization assay (see above, Figure 2). Overall, these structural analyses indicate that RBD rotational flexibility

and acquisition of quaternary interactions can play an important role in CR3022 interaction with the S protein. CR3022 adds to the growing list of neutralization antibodies that can utilize quaternary interactions for binding to the S protein [12, 36].

DISCUSSION

While it is now known that SARS-CoV and SARS-CoV-2 differ in antigenicity despite relatively high sequence conservation [1, 3, 4, 14], there is a paucity of understanding of the underlying molecular determinants of these antigenic changes and the structural consequences of these differences. Through structural analysis of the CR3022-RBD complex and mutagenesis experiments, we show that a single amino-acid substitution at residue 384 contributes to an important antigenic difference in a highly conserved (neutralizing) epitope between SARS-CoV-2 and SARS-CoV.

While CR3022 cannot neutralize SARS-CoV-2 WT in almost all studies [3, 5, 20, 22], it can neutralize the SARS-CoV-2 P384A mutant. The K_D of CR3022 Fab to SARS-CoV-2 WT RBD is 68 nM, whereas to SARS-CoV-2 P384A RBD is 1 nM (Figure 1B-C), indicating that the affinity threshold for neutralization of SARS-CoV-2 to this epitope is in the low nM range. However, despite having a low nM affinity to SARS-CoV-2 P384A RBD, CR3022 only weakly neutralizes SARS-CoV-2 P384A with an IC_{50} of 3.2 μg/ml and SARS-CoV with an IC_{50} of 5.2 μg/ml. In contrast, antibodies with similar or less Fab binding affinity to other RBD epitopes, such as the receptor binding site, can neutralize SARS-CoV-2 much more efficiently. For example, previously characterized SARS-CoV-2 antibodies CC12.1 and CC12.3, which have a K_D to SARS-CoV-2 RBD of 17 nM and 14 nM respectively, neutralize SARS-CoV-2 at an IC_{50} of ~20 ng/ml [3, 37]. Of note, the K_D and IC_{50} of CC12.1 and CC12.3 were measured in the same manner as this study. The lack of correlation between affinity and neutralizing activity is therefore not due to the difference in the assays

between studies. In fact, a previous study also demonstrated a lack of correlation between RBD binding and neutralization for monoclonal antibodies [3]. Together, these observations suggest that the affinity threshold for SARS-CoV-2 neutralization by RBD-targeting antibodies may be epitope dependent. The difference in affinity threshold for different epitopes is also likely to be related not only in the ability to block ACE2-binding [3, 38], but also in antibody avidity where bivalent binding can cross-link different RBD domains on the same or different spikes and, hence, substantially enhance binding and neutralization [23].

Given the scale of the outbreak, SARS-CoV-2 may persist and circulate in humans for years to come [39]. A number of SARS-CoV-2 vaccine candidates are currently under clinical trials (https://clinicaltrials.gov/ct2/who_table) [40], which offer a potential solution to alleviate the global health and socio-economic devastation bought by SARS-CoV-2. However, whether SARS-CoV-2 can escape vaccine-induced immunity through antigenic drift remains to be determined, although escape mutations to many monoclonal antibodies have been tested *in vitro* [2]. Identification of the key residues that are responsible for differences in antigenicity among SARS-CoV-2, SARS-CoV, and possibly other SARS-related viruses, should provide a starting point to understand the potential for antigenic drift in SARS-like coronaviruses. The ongoing efforts in SARS-CoV-2 antibody discovery and structural characterization will therefore advance our molecular understanding of antigenic variation in SARS-like CoVs, and consequences for vaccine and therapeutic design, especially to cross-neutralizing epitopes.

ACKNOWLEDGEMENTS

We thank Henry Tien for technical support with the crystallization robot, Jeanne Matteson for contribution to mammalian cell culture, Wenli Yu to insect cell culture, Robyn Stanfield

for assistance in data collection, and Chris Mok for pilot testing of the pseudovirus assay. We are grateful to the staff of Stanford Synchrotron Radiation Laboratory (SSRL) Beamline 12-2 for assistance. This work was supported by NIH R00 AI139445 (N.C.W.), NIH R01 AI073148 (D.N.), the Bill and Melinda Gates Foundation OPP1170236 (A.B.W. and I.A.W.) and NIH CHAVD UM1 AI44462 (A.B.W. and I.A.W.). Use of the SSRL, SLAC National Accelerator Laboratory, is supported by the U.S. Department of Energy, Office of Science, Office of Basic Energy Sciences under Contract No. DE-AC02–76SF00515. The SSRL Structural Molecular Biology Program is supported by the DOE Office of Biological and Environmental Research, and by the National Institutes of Health, National Institute of General Medical Sciences (including P41GM103393).

AUTHOR CONTRIBUTIONS

N.C.W., M.Y., D.H., S.B., A.B.W and I.A.W. conceived and designed the study. N.C.W., M.Y., C.C.D.L. and S.B. expressed and purified the proteins. M.Y. performed biolayer interferometry binding assays. N.C.W. and M.Y. performed the crystallization experiment and X.Z. collected the X-ray data. M.Y. determined and refined the X-ray structures. S.B. and H.L.T. performed the negative-stain electron microscopy. D.H., L.P., L.Y. and D.N. performed the pseudovirus neutralization assay. N.C.W., M.Y., D.H., S.B., A.B.W. and I.A.W. analyzed the data. N.C.W., M.Y. and I.A.W. wrote the paper and all authors reviewed and edited the paper.

DECLARATION OF INTERESTS

The authors declare no competing interests.

MATERIALS AND METHODS

Expression and purification of SARS-CoV RBD

RBD (residues: 306-527) of the SARS-CoV spike (S) protein (GenBank: ABF65836.1) was fused with an N-terminal gp67 signal peptide and a C-terminal His_6 tag, and cloned into a customized pFastBac vector [41]. Recombinant bacmid DNA was generated using the Bac-to-Bac system (Thermo Fisher Scientific). Baculovirus was generated by transfecting purified bacmid DNA into Sf9 cells using FuGENE HD (Promega), and subsequently used to infect suspension cultures of High Five cells (Thermo Fisher Scientific) at an MOI of 5 to 10. Infected High Five cells were incubated at 28 °C with shaking at 110 r.p.m. for 72 h for protein expression. The supernatant was then concentrated using a 10 kDa MW cutoff Centramate cassette (Pall Corporation). SARS-CoV RBD protein was purified by Ni-NTA, followed by size exclusion chromatography, and buffer exchanged into 20 mM Tris-HCl pH 7.4 and 150 mM NaCl.

Expression and purification of SARS-CoV spike

The SARS-CoV spike construct (Tor2 strain) for recombinant spike protein expression contains the mammalian-codon-optimized gene encoding residues 1-1190 of the spike followed by a C-terminal T4 fibritin trimerization domain, a HRV3C cleavage site, 8x-His tag and a Twin-strep tags subcloned into the eukaryotic-expression vector pαH. Residues at 968 and 969 were replaced by prolines for generating stable spike proteins as described previously [28]. The spike plasmid was transfected into FreeStyle 293F cells and cultures were harvested at 6-day post-transfection. Proteins were purified from the supernatants on His-Complete columns using a 250 mM imidazole elution buffer. The elution was buffer exchanged to Tris-NaCl buffer (25 mM Tris, 500 mM NaCl, pH 7.4) before further purification using Superose 6 increase 10/300 column (GE Healthcare). Protein fractions corresponding to the trimeric spike proteins were collected and concentrated.

322

323 **Expression and purification of CR3022 Fab**

324 The CR3022 Fab heavy (GenBank: DQ168569.1) and light (GenBank: DQ168570.1)
325 chains were cloned into phCMV3. The plasmids were transiently co-transfected into
326 Expi293F cells at a ratio of 2:1 (HC:LC) using ExpiFectamine™ 293 Reagent (Thermo
327 Fisher Scientific) according to the manufacturer's instructions. The supernatant was
328 collected at 7 days post-transfection. The Fab was purified with a CaptureSelect™ CH1-
329 XL Pre-packed Column (Thermo Fisher Scientific) followed by size exclusion
330 chromatography. For crystallization, a VSRRLP variant of the elbow region was used to
331 reduce the conformational flexibility between the constant and variable domains [25].

332

333 **Crystallization and structural determination**

334 Purified CR3022 Fab with a VSRRLP modification in the elbow region and SARS-CoV
335 RBD were mixed at a molar ratio of 1:1 and incubated overnight at 4°C. The complex (7.5
336 mg/ml) was screened for crystallization using the 384 conditions of the JCSG Core Suite
337 (Qiagen) on our custom-designed robotic CrystalMation system (Rigaku) at Scripps
338 Research by the vapor diffusion method in sitting drops containing 0.1 µl of protein and
339 0.1 µl of reservoir solution. Optimized crystals were then grown in 2 M sodium chloride
340 and 10% PEG 6000 at 4°C. Crystals were grown for 7 days and then flash cooled in liquid
341 nitrogen. Diffraction data were collected at cryogenic temperature (100 K) at Stanford
342 Synchrotron Radiation Lightsource (SSRL) beamline 12-2 with a wavelength of 1.033 Å,
343 and processed with HKL2000 [42]. Structures were solved by molecular replacement
344 using PHASER [43] with PDB 6W41 for CR3022 Fab [20] and PDB 2AJF for SARS-CoV
345 RBD [44]. Iterative model building and refinement were carried out in COOT [45] and
346 PHENIX [46], respectively. Ramachandran statistics were calculated using MolProbity
347 [47].

348

349 **Negative-stain electron microscopy**

350 Six molar excess of CR3022 Fab (unmodified) was added to SARS-CoV spike protein 1
351 hour prior to direct deposition onto carbon-coated 400-mesh copper grids. The grids were
352 stained with 2 % (w/v) uranyl-formate for 90 seconds immediately following sample
353 application. Grids were imaged on Tecnai T12 Spirit at 120 keV with a 4k x 4k Eagle CCD.
354 Micrographs were collected using Leginon [48] and images were transferred to Appion
355 [49] for particle picking using a difference-of-Gaussians picker (DoG-picker) [50] and
356 generation of particle stacks. Particle stacks were further transferred to Relion [51] for 2D
357 classification followed by 3D classification to select good classes. Select 3D classes were
358 auto-refined on Relion and used for making figures using UCSF Chimera [52].

359

360 **Cryo-EM sample preparation**

361 SARS-CoV spike protein was incubated with six molar excess of CR3022 Fab for 2 h. 3.5
362 µL of the complex (0.9 mg/ml) was mixed with 0.5 µL of 0.04 mM lauryl maltose neopentyl
363 glycol (LMNG) solution immediately before sample deposition onto a 1.2/1.3 300-Gold grid
364 (EMS). The grids were plasma cleaned for 7 seconds using a Gatan Solarus 950 Plasma
365 system prior to sample deposition. Following sample application, grids were blotted for 3
366 seconds before being vitrified in liquid ethane using a Vitrobot Mark IV (Thermo Fisher).

367

368 **Cryo-EM data collection and processing**

369 Data collection was performed using a Talos Arctica TEM at 200 kV with a Gatan K2
370 Summit detector at a magnification of 36,000x, resulting in a 1.15 Å pixel size. Total
371 exposure was split into 250 ms frames with a total cumulative dose of ~50 $e^-/Å^2$.
372 Micrographs were collected through Leginon software at a nominal defocus range of -0.4
373 µm to -1.6 µm and MotionCor2 was used for alignment and dose weighting of the frames

[48, 53]. Micrographs were transferred to CryoSPARC 2.9 for further processing [54]. CTF estimations were performed using GCTF and micrographs were selected using the Curate Exposures tool in CryoSPARC based on their CTF resolution estimates (cutoff 5 Å) for downstream particle picking, extraction and iterative rounds of 2D classification and selection [55]. Particles selected from 2D classes were transferred to Relion 3.1 for direct C3 refinement, symmetry expansion of particles and iterative rounds of 3D focused classification using spherical masks around the RBD and Fab [51]. Final subsets of clean particles from 4 different classes were each refined with C1 symmetry. Figures were generated using UCSF Chimera and UCSF Chimera X [52].

Calculation of rotation angles

Comparisons of subunit rotation angles among different structures were performed with a software 'Superpose' in the CCP4 package [56, 57]. For each classified conformation, the Cα atoms of the RBD domain are superimposed to the equivalent atoms of the RBD in "up"-conformation in a previously reported spike trimer cryoEM structure (PDB 6ACD) [35]. The rotation matrices generated by superposing each pair of structures with 'Superpose' were adopted to calculate the subunit rotation angle following the equation shown as below:

$$\theta = \cos^{-1}\frac{X_{11} + Y_{22} + Z_{33} - 1}{2}$$

where θ is the subunit rotation angle, X_{11}, Y_{22}, and Z_{33} represent the X_{11}, Y_{22}, and Z_{33} values in the rotation matrix calculated for the superpose.

Biolayer interferometry binding assay

Binding assays were performed by biolayer interferometry (BLI) using an Octet Red instrument (FortéBio) as described previously [58]. Briefly, His_6-tagged SARS-CoV RBD

proteins at 20 to 100 μg/ml in 1x kinetics buffer (1x PBS, pH 7.4, 0.01% BSA and 0.002% Tween 20) were loaded onto Anti-Penta-HIS (HIS1K) biosensors and incubated with the indicated concentrations of CR3022 Fab. The assay consisted of five steps: 1) baseline: 60 s with 1x kinetics buffer; 2) loading: 300 s with His_6-tagged S or RBD proteins; 3) baseline: 60 s with 1x kinetics buffer; 4) association: 120 s with samples (Fab or IgG); and 5) dissociation: 120 s with 1x kinetics buffer. For estimating the exact K_D, a 1:1 binding model was used.

Pseudovirus neutralization assay

Pseudovirus preparation and assay were performed as previously described [3]. Briefly, MLV-gag/pol and MLV-CMV plasmids was co-transfected into HEK293T cells along with full-length or P384A SARS-CoV-2 spike plasmids using Lipofectamine 2000 to produce pseudoviruses competent for single-round infection. The supernatant containing MLV-pseudotyped viral particles was collected at 48 hours post transfection, aliquoted and frozen at -80°C until used. For each well in a 96-well half-area plate, 25 μl of virus was immediately mixed with 25 μl of serially diluted IgG or Fab, and incubated for 1 hour at 37°C. For each well, 10,000 HeLa-hACE2 cells in 50 μl of media supplemented with 20 μg/ml dextran were added to the antibody-virus mixture. The 96-well half-area plate was then incubated at 37°C. At 42 to 48 hours post-infection, HeLa-hACE2 cells were lysed using 1x luciferase lysis buffer (25 mM Gly-Gly pH 7.8, 15 mM $MgSO_4$, 4 mM EGTA, and 1% Triton X-100). Luciferase intensity was then measured using Bright-Glo Luciferase Assay System (Promega) according to the manufacturer's instructions. Percentage of neutralization was calculated using the following equation:

$$\%\, neutralization = 100 \times \left(1 - \frac{RULs\ of\ sample - Average\ RULs\ of\ Background}{Average\ of\ RULs\ of\ Virus\ only\ contrl - Average\ RULs\ of\ Backgroud}\right)$$

DATA AVAILABILITY

The X-ray coordinates and structure factors have been deposited to the RCSB Protein Data Bank under accession code: 7JN5. The EM maps will be deposited in the Electron Microscopy Data Bank (EMDB).

REFERENCES

1. Brouwer PJM, Caniels TG, van der Straten K, Snitselaar JL, Aldon Y, Bangaru S, et al. Potent neutralizing antibodies from COVID-19 patients define multiple targets of vulnerability. Science. 2020;369(6504):643-50. doi: 10.1126/science.abc5902.

2. Baum A, Fulton BO, Wloga E, Copin R, Pascal KE, Russo V, et al. Antibody cocktail to SARS-CoV-2 spike protein prevents rapid mutational escape seen with individual antibodies. Science. 2020;369(6506):1014-8. Epub 2020/06/17. doi: 10.1126/science.abd0831. PubMed PMID: 32540904; PubMed Central PMCID: PMC7299283.

3. Rogers TF, Zhao F, Huang D, Beutler N, Burns A, He W-t, et al. Isolation of potent SARS-CoV-2 neutralizing antibodies and protection from disease in a small animal model. Science. 2020;369(6506):956-63. doi: 10.1126/science.abc7520.

4. Ju B, Zhang Q, Ge J, Wang R, Sun J, Ge X, et al. Human neutralizing antibodies elicited by SARS-CoV-2 infection. Nature. 2020;584(7819):115-9. Epub 2020/05/27. doi: 10.1038/s41586-020-2380-z. PubMed PMID: 32454513.

5. Chi X, Yan R, Zhang J, Zhang G, Zhang Y, Hao M, et al. A neutralizing human antibody binds to the N-terminal domain of the Spike protein of SARS-CoV-2. Science. 2020;368(6504):1274-8. doi: 10.1126/science.abc6952.

6. Wec AZ, Wrapp D, Herbert AS, Maurer D, Haslwanter D, Sakharkar M, et al. Broad neutralization of SARS-related viruses by human monoclonal antibodies. Science. 2020;369(6504):731-6. doi: 10.1126/science.abc7424.

7. Pinto D, Park YJ, Beltramello M, Walls AC, Tortorici MA, Bianchi S, et al. Cross-neutralization of SARS-CoV-2 by a human monoclonal SARS-CoV antibody. Nature. 2020;583(7815):290-5. Epub 2020/05/19. doi: 10.1038/s41586-020-2349-y. PubMed PMID: 32422645.

8. Zost SJ, Gilchuk P, Case JB, Binshtein E, Chen RE, Nkolola JP, et al. Potently neutralizing and protective human antibodies against SARS-CoV-2. Nature. 2020;584(7821):443-9. Epub 2020/07/16. doi: 10.1038/s41586-020-2548-6. PubMed PMID: 32668443.

9. Cao Y, Su B, Guo X, Sun W, Deng Y, Bao L, et al. Potent neutralizing antibodies against SARS-CoV-2 identified by high-throughput single-cell sequencing of convalescent patients' B cells. Cell. 2020;182(1):73-84. Epub 2020/05/20. doi: 10.1016/j.cell.2020.05.025. PubMed PMID: 32425270; PubMed Central PMCID: PMC7231725.

10. Seydoux E, Homad LJ, MacCamy AJ, Parks KR, Hurlburt NK, Jennewein MF, et al. Analysis of a SARS-CoV-2-infected individual reveals development of potent neutralizing antibodies with limited somatic mutation. Immunity. 2020;53(1):98-105. doi: 10.1101/2020.05.12.091298.

11. Shi R, Shan C, Duan X, Chen Z, Liu P, Song J, et al. A human neutralizing antibody targets the receptor binding site of SARS-CoV-2. Nature. 2020;584(7819):120-4. Epub 2020/05/27. doi: 10.1038/s41586-020-2381-y. PubMed PMID: 32454512.

12. Liu L, Wang P, Nair MS, Yu J, Rapp M, Wang Q, et al. Potent neutralizing antibodies directed to multiple epitopes on SARS-CoV-2 spike. Nature. 2020;584(7821):450-6. Epub 2020/07/23. doi: 10.1038/s41586-020-2571-7. PubMed PMID: 32698192.

13. Zhou P, Yang XL, Wang XG, Hu B, Zhang L, Zhang W, et al. A pneumonia outbreak associated with a new coronavirus of probable bat origin. Nature. 2020;579(7798):270-3. Epub 2020/02/06. doi: 10.1038/s41586-020-2012-7. PubMed PMID: 32015507.

14. Lv H, Wu NC, Tsang OT-Y, Yuan M, Perera RAPM, Leung WS, et al. Cross-reactive antibody response between SARS-CoV-2 and SARS-CoV infections. Cell Rep. 2020;31(9):107725. doi: 10.1016/j.celrep.2020.107725.

15. Ou X, Liu Y, Lei X, Li P, Mi D, Ren L, et al. Characterization of spike glycoprotein of SARS-CoV-2 on virus entry and its immune cross-reactivity with SARS-CoV. Nat Commun. 2020;11(1):1620. Epub 2020/03/30. doi: 10.1038/s41467-020-15562-9. PubMed PMID: 32221306; PubMed Central PMCID: PMC7100515.

16. Wang C, Li W, Drabek D, Okba NMA, van Haperen R, Osterhaus ADME, et al. A human monoclonal antibody blocking SARS-CoV-2 infection. Nat Commun. 2020;11(1):2251. doi: 10.1101/2020.03.11.987958.

17. Zhou D, Duyvesteyn HME, Chen C-P, Huang C-G, Chen T-H, Shih S-R, et al. Structural basis for the neutralization of SARS-CoV-2 by an antibody from a convalescent patient. Nat Struct Mol Biol. 2020. doi: 10.1038/s41594-020-0480-y.

18. ter Meulen J, van den Brink EN, Poon LL, Marissen WE, Leung CS, Cox F, et al. Human monoclonal antibody combination against SARS coronavirus: synergy and coverage of escape mutants. PLoS Med. 2006;3(7):e237. Epub 2006/06/27. doi: 10.1371/journal.pmed.0030237. PubMed PMID: 16796401; PubMed Central PMCID: PMC1483912.

19. Tian X, Li C, Huang A, Xia S, Lu S, Shi Z, et al. Potent binding of 2019 novel coronavirus spike protein by a SARS coronavirus-specific human monoclonal antibody. Emerg Microbes Infect. 2020;9(1):382-5. Epub 2020/02/18. doi: 10.1080/22221751.2020.1729069. PubMed PMID: 32065055.

20. Yuan M, Wu NC, Zhu X, Lee CD, So RTY, Lv H, et al. A highly conserved cryptic epitope in the receptor-binding domains of SARS-CoV-2 and SARS-CoV. Science. 2020;368(6491):630-3. Epub 2020/04/05. doi: 10.1126/science.abb7269. PubMed PMID: 32245784.

21. Liu H, Wu NC, Yuan M, Bangaru S, Torres JL, Caniels TG, et al. Cross-neutralization of a SARS-CoV-2 antibody to a functionally conserved site is mediated by avidity. bioRxiv. doi: 10.1101/2020.08.02.233536.

22. Yi C, Sun X, Ye J, Ding L, Liu M, Yang Z, et al. Key residues of the receptor binding motif in the spike protein of SARS-CoV-2 that interact with ACE2 and neutralizing antibodies. Cell Mol Immunol. 2020;17(6):621-30. Epub 2020/05/18. doi: 10.1038/s41423-020-0458-z. PubMed PMID: 32415260; PubMed Central PMCID: PMC7227451.

23. Barnes CO, West AP, Huey-Tubman KE, Hoffmann MAG, Sharaf NG, Hoffman PR, et al. Structures of human antibodies bound to SARS-CoV-2 spike reveal common epitopes and recurrent features of antibodies. Cell. 2020;182(4):828-42. doi: 10.1016/j.cell.2020.06.025.

24. Li W, Shi Z, Yu M, Ren W, Smith C, Epstein JH, et al. Bats are natural reservoirs of SARS-like coronaviruses. Science. 2005;310(5748):676-9. Epub 2005/10/01. doi: 10.1126/science.1118391. PubMed PMID: 16195424.

25. Bailey LJ, Sheehy KM, Dominik PK, Liang WG, Rui H, Clark M, et al. Locking the elbow: improved antibody Fab fragments as chaperones for structure determination. J Mol Biol. 2018;430(3):337-47. Epub 2017/12/24. doi: 10.1016/j.jmb.2017.12.012. PubMed PMID: 29273204; PubMed Central PMCID: PMC5800945.

26. Gui M, Song W, Zhou H, Xu J, Chen S, Xiang Y, et al. Cryo-electron microscopy structures of the SARS-CoV spike glycoprotein reveal a prerequisite conformational state for receptor binding. Cell Res. 2017;27(1):119-29. Epub 2016/12/23. doi: 10.1038/cr.2016.152. PubMed PMID: 28008928; PubMed Central PMCID: PMC5223232.

27. Yuan Y, Cao D, Zhang Y, Ma J, Qi J, Wang Q, et al. Cryo-EM structures of MERS-CoV and SARS-CoV spike glycoproteins reveal the dynamic receptor binding domains. Nat Commun. 2017;8:15092. Epub 2017/04/11. doi: 10.1038/ncomms15092. PubMed PMID: 28393837; PubMed Central PMCID: PMC5394239.

28. Kirchdoerfer RN, Wang N, Pallesen J, Wrapp D, Turner HL, Cottrell CA, et al. Stabilized coronavirus spikes are resistant to conformational changes induced by receptor recognition or proteolysis. Sci Rep. 2018;8(1):15701. Epub 2018/10/26.

doi: 10.1038/s41598-018-34171-7. PubMed PMID: 30356097; PubMed Central PMCID: PMC6200764.

29. Huo J, Zhao Y, Ren J, Zhou D, Duyvesteyn HME, Ginn HM, et al. Neutralization of SARS-CoV-2 by destruction of the prefusion spike. Cell Host Microbe. 2020. Epub 2020/06/26. doi: 10.1016/j.chom.2020.06.010. PubMed PMID: 32585135; PubMed Central PMCID: PMC7303615.

30. Wrapp D, Wang N, Corbett KS, Goldsmith JA, Hsieh CL, Abiona O, et al. Cryo-EM structure of the 2019-nCoV spike in the prefusion conformation. Science. 2020;367(6483):1260-3. Epub 2020/02/23. doi: 10.1126/science.abb2507. PubMed PMID: 32075877.

31. Walls AC, Park YJ, Tortorici MA, Wall A, McGuire AT, Veesler D. Structure, function, and antigenicity of the SARS-CoV-2 spike glycoprotein. Cell. 2020;181(2):281-92.e6. Epub 2020/03/11. doi: 10.1016/j.cell.2020.02.058. PubMed PMID: 32155444.

32. Cai Y, Zhang J, Xiao T, Peng H, Sterling SM, Walsh RM, Jr., et al. Distinct conformational states of SARS-CoV-2 spike protein. Science. 2020. Epub 2020/07/23. doi: 10.1126/science.abd4251. PubMed PMID: 32694201.

33. Ke Z, Oton J, Qu K, Cortese M, Zila V, McKeane L, et al. Structures and distributions of SARS-CoV-2 spike proteins on intact virions. Nature. 2020. doi: 10.1038/s41586-020-2665-2.

34. Yao H, Song Y, Chen Y, Wu N, Xu J, Sun C, et al. Molecular architecture of the SARS-CoV-2 virus. bioRxiv. 2020. doi: 10.1101/2020.07.08.192104.

35. Song W, Gui M, Wang X, Xiang Y. Cryo-EM structure of the SARS coronavirus spike glycoprotein in complex with its host cell receptor ACE2. PLoS Pathog. 2018;14(8):e1007236. Epub 2018/08/14. doi: 10.1371/journal.ppat.1007236. PubMed PMID: 30102747; PubMed Central PMCID: PMC6107290.

36. Barnes CO, Jette CA, Abernathy ME, Dam K-MA, Esswein SR, Gristick HB, et al. Structural classification of neutralizing antibodies against the SARS-CoV-2 spike receptor-binding domain suggests vaccine and therapeutic strategies. bioRxiv. 2020. doi: 10.1101/2020.08.30.273920.

37. Yuan M, Liu H, Wu NC, Lee C-CD, Zhu X, Zhao F, et al. Structural basis of a shared antibody response to SARS-CoV-2. Science. 2020;369(6507):1119-23. doi: 10.1101/2020.06.08.141267. PubMed PMID: 32661058; PubMed Central PMCID: PMC716439.

38. Tan CW, Chia WN, Qin X, Liu P, Chen MI, Tiu C, et al. A SARS-CoV-2 surrogate virus neutralization test based on antibody-mediated blockage of ACE2-spike protein-protein interaction. Nat Biotechnol. 2020;38:1073-8. Epub 2020/07/25. doi: 10.1038/s41587-020-0631-z. PubMed PMID: 32704169.

39. Kissler SM, Tedijanto C, Goldstein E, Grad YH, Lipsitch M. Projecting the transmission dynamics of SARS-CoV-2 through the postpandemic period.

Science. 2020;368(6493):860-8. Epub 2020/04/16. doi: 10.1126/science.abb5793. PubMed PMID: 32291278; PubMed Central PMCID: PMC7164482.

40. Amanat F, Krammer F. SARS-CoV-2 vaccines: status report. Immunity. 2020;52(4):583-9. Epub 2020/04/08. doi: 10.1016/j.immuni.2020.03.007. PubMed PMID: 32259480; PubMed Central PMCID: PMC7136867.

41. Ekiert DC, Friesen RH, Bhabha G, Kwaks T, Jongeneelen M, Yu W, et al. A highly conserved neutralizing epitope on group 2 influenza A viruses. Science. 2011;333(6044):843-50. doi: 10.1126/science.1204839. PubMed PMID: 21737702; PubMed Central PMCID: PMC3210727.

42. Otwinowski Z, Minor W. Processing of X-ray diffraction data collected in oscillation mode. Methods Enzymol. 1997;276:307-26. Epub 1997/01/01. PubMed PMID: 27754618.

43. McCoy AJ, Grosse-Kunstleve RW, Adams PD, Winn MD, Storoni LC, Read RJ. Phaser crystallographic software. J Appl Crystallogr. 2007;40(Pt 4):658-74. doi: 10.1107/S0021889807021206. PubMed PMID: 19461840; PubMed Central PMCID: PMC2483472.

44. Li F, Li W, Farzan M, Harrison SC. Structure of SARS coronavirus spike receptor-binding domain complexed with receptor. Science. 2005;309(5742):1864-8. Epub 2005/09/17. doi: 10.1126/science.1116480. PubMed PMID: 16166518.

45. Emsley P, Lohkamp B, Scott WG, Cowtan K. Features and development of Coot. Acta Crystallogr D Biol Crystallogr. 2010;66(Pt 4):486-501. doi: 10.1107/S0907444910007493. PubMed PMID: 20383002; PubMed Central PMCID: PMC2852313.

46. Adams PD, Afonine PV, Bunkoczi G, Chen VB, Davis IW, Echols N, et al. PHENIX: a comprehensive Python-based system for macromolecular structure solution. Acta Crystallogr D Biol Crystallogr. 2010;66(Pt 2):213-21. Epub 2010/02/04. doi: 10.1107/S0907444909052925. PubMed PMID: 20124702; PubMed Central PMCID: PMC2815670.

47. Chen VB, Arendall WB, 3rd, Headd JJ, Keedy DA, Immormino RM, Kapral GJ, et al. MolProbity: all-atom structure validation for macromolecular crystallography. Acta Crystallogr D Biol Crystallogr. 2010;66(Pt 1):12-21. doi: 10.1107/S0907444909042073. PubMed PMID: 20057044; PubMed Central PMCID: PMC2803126.

48. Suloway C, Pulokas J, Fellmann D, Cheng A, Guerra F, Quispe J, et al. Automated molecular microscopy: the new Leginon system. J Struct Biol. 2005;151(1):41-60. Epub 2005/05/14. doi: 10.1016/j.jsb.2005.03.010. PubMed PMID: 15890530.

49. Lander GC, Stagg SM, Voss NR, Cheng A, Fellmann D, Pulokas J, et al. Appion: an integrated, database-driven pipeline to facilitate EM image processing. J

Struct Biol. 2009;166(1):95-102. PubMed PMID: 19263523; PubMed Central PMCID: PMC2775544.

50. Voss NR, Yoshioka CK, Radermacher M, Potter CS, Carragher B. DoG Picker and TiltPicker: software tools to facilitate particle selection in single particle electron microscopy. J Struct Biol. 2009;166(2):205-13. PubMed PMID: 19374019; PubMed Central PMCID: PMC2768396.

51. Zivanov J, Nakane T, Forsberg BO, Kimanius D, Hagen WJ, Lindahl E, et al. New tools for automated high-resolution cryo-EM structure determination in RELION-3. eLife. 2018;7:e42166 Epub 2018/11/10. doi: 10.7554/eLife.42166. PubMed PMID: 30412051; PubMed Central PMCID: PMC6250425.

52. Pettersen EF, Goddard TD, Huang CC, Couch GS, Greenblatt DM, Meng EC, et al. UCSF Chimera--a visualization system for exploratory research and analysis. J Comput Chem. 2004;25(13):1605-12. Epub 2004/07/21. doi: 10.1002/jcc.20084. PubMed PMID: 15264254.

53. Zheng SQ, Palovcak E, Armache JP, Verba KA, Cheng Y, Agard DA. MotionCor2: anisotropic correction of beam-induced motion for improved cryo-electron microscopy. Nat Methods. 2017;14(4):331-2. Epub 2017/03/03. doi: 10.1038/nmeth.4193. PubMed PMID: 28250466; PubMed Central PMCID: PMC5494038.

54. Punjani A, Rubinstein JL, Fleet DJ, Brubaker MA. cryoSPARC: algorithms for rapid unsupervised cryo-EM structure determination. Nat Methods. 2017;14(3):290-6. Epub 2017/02/07. doi: 10.1038/nmeth.4169. PubMed PMID: 28165473.

55. Zhang K. Gctf: Real-time CTF determination and correction. J Struct Biol. 2016;193(1):1-12. Epub 2015/11/26. doi: 10.1016/j.jsb.2015.11.003. PubMed PMID: 26592709; PubMed Central PMCID: PMC4711343.

56. Winn MD, Ballard CC, Cowtan KD, Dodson EJ, Emsley P, Evans PR, et al. Overview of the CCP4 suite and current developments. Acta Crystallogr D Biol Crystallogr. 2011;67(Pt 4):235-42. Epub 2011/04/05. doi: 10.1107/S0907444910045749. PubMed PMID: 21460441; PubMed Central PMCID: PMC3069738.

57. Krissinel E, Henrick K. Secondary-structure matching (SSM), a new tool for fast protein structure alignment in three dimensions. Acta Crystallogr D Biol Crystallogr. 2004;60(Pt 12 Pt 1):2256-68. Epub 2004/12/02. doi: 10.1107/S0907444904026460. PubMed PMID: 15572779.

58. Wu NC, Grande G, Turner HL, Ward AB, Xie J, Lerner RA, et al. In vitro evolution of an influenza broadly neutralizing antibody is modulated by hemagglutinin receptor specificity. Nat Commun. 2017;8:15371. doi: 10.1038/ncomms15371. PubMed PMID: 28504265; PubMed Central PMCID: PMC5440694.

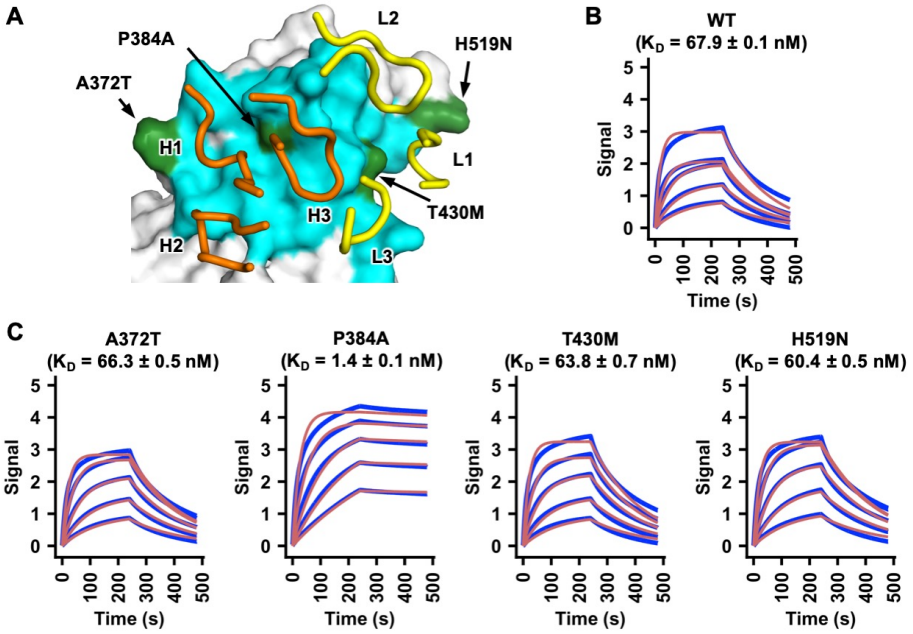

Figure 1. A single P384A substitution increases CR3022 affinity to the SARS-CoV-2 RBD. (A) Epitope residues on SARS-CoV RBD are colored in cyan and green. The CR3022 CDR loops that contact the RBD are shown and labeled. Cyan: epitope residues that are conserved between SARS-CoV-2 and SARS-CoV. Green: epitope residues that are not conserved between SARS-CoV-2 and SARS-CoV. Orange: CR3022 heavy chain. Yellow: CR3022 light chain. **(B-C)** Binding of CR3022 Fab to **(B)** wild-type (WT) SARS-CoV-2 RBD and **(C)** different mutants was measured by biolayer interferometry with RBD loaded on the biosensor and Fab in solution. Y-axis represents the response. Dissociation constants (K_D) for the Fab were obtained using a 1:1 binding model, respectively, which is represented by the red curves. Representative results of two replicates for each experiment are shown. Of note, mammalian cell-expressed RBD was used in the binding experiments in this study, whereas insect cell-expressed RBD was used in our previous study [20]. This difference may explain the slight discrepancy in the K_D of CR3022 Fab to SARS-CoV-2 RBD WT between this study and our previous study [20].

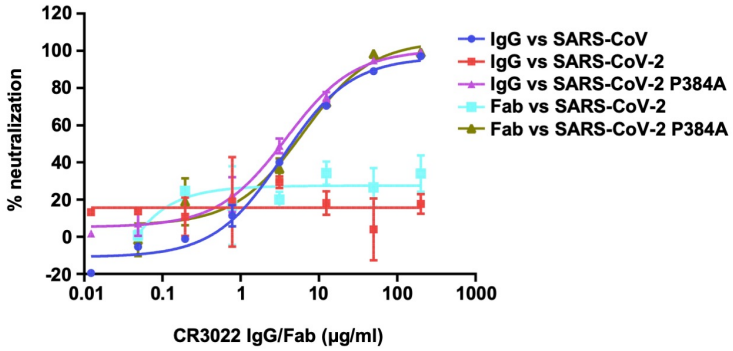

678

679 **Figure 2. Pseudovirus neutralization assay.** The neutralizing activity of CR3022 IgG or

680 Fab to SARS-CoV, SARS-CoV-2, and SARS-CoV-2 P384A mutant was measured in a

681 pseudovirus neutralization assay.

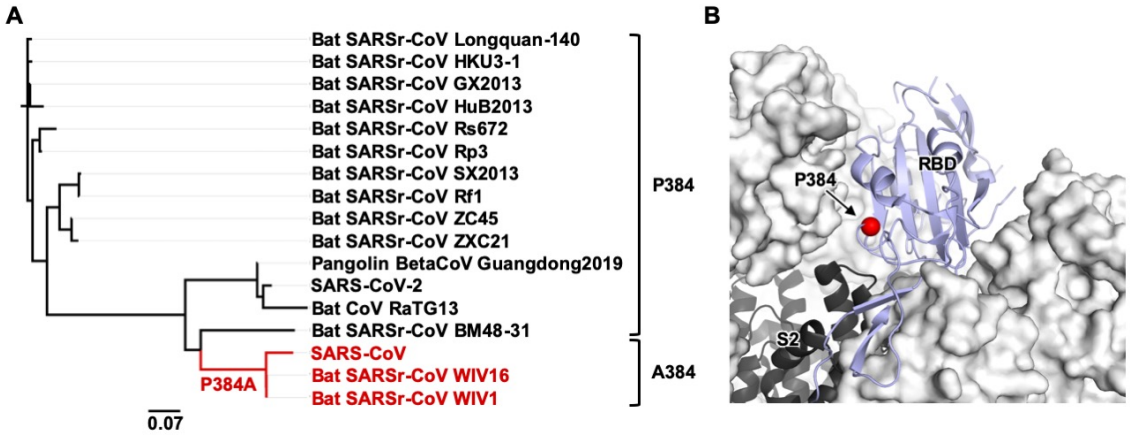

682

683 **Figure 3. Sequence conservation and location of residue 384. (A)** A phylogenetic tree
684 was constructed based on the amino-acid sequences of RBDs from SARS-CoV-2, SARS-
685 CoV, and SARS-related coronavirus (SARSr-CoV) strains. Branches corresponding to
686 strains that have A384 are colored in red on the phylogenetic tree. Scale bar represents
687 0.07 amino-acid substitutions per position. **(B)** The location of P384 is shown on the
688 SARS-CoV-2 S protein (PDB 6VXX [31]). S1 domain is represented by the white surface
689 and the S2 domain by the black cartoon. The location of residue 384 is indicated by the
690 red sphere on the RBD in the “down” conformation (blue cartoon).

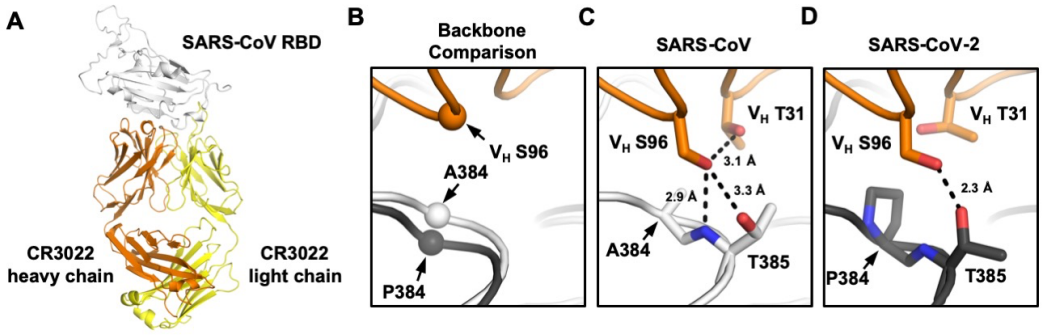

691

692 **Figure 4. Crystal structure of CR3022 in complex with SARS-CoV RBD. (A)** Crystal
693 structure of CR3022 Fab in complex with SARS-CoV RBD. CR3022 heavy chain is colored
694 in orange, CR3022 light chain in yellow, and SARS-CoV-2 RBD in light grey. **(B)** Structures
695 of CR3022 in complex with SARS-CoV-2 RBD and with SARS-CoV RBD were aligned
696 using the CR3022 heavy chain variable domain and the region around residue 384 is
697 shown. Orange: CR3022 heavy chain. White: SARS-CoV RBD. Dark gray: SARS-CoV-2
698 RBD. The Cαs of S96 on CR3022 heavy chain, A384 on SARS-CoV RBD, and P384 on
699 SARS-CoV-2 RBD are shown in sphere representation. **(C-D)** Interaction between
700 CR3022 and residue 384 on **(C)** SARS-CoV RBD, and **(D)** SARS-CoV-2 RBD. Hydrogen
701 bonds are represented by dashed lines.

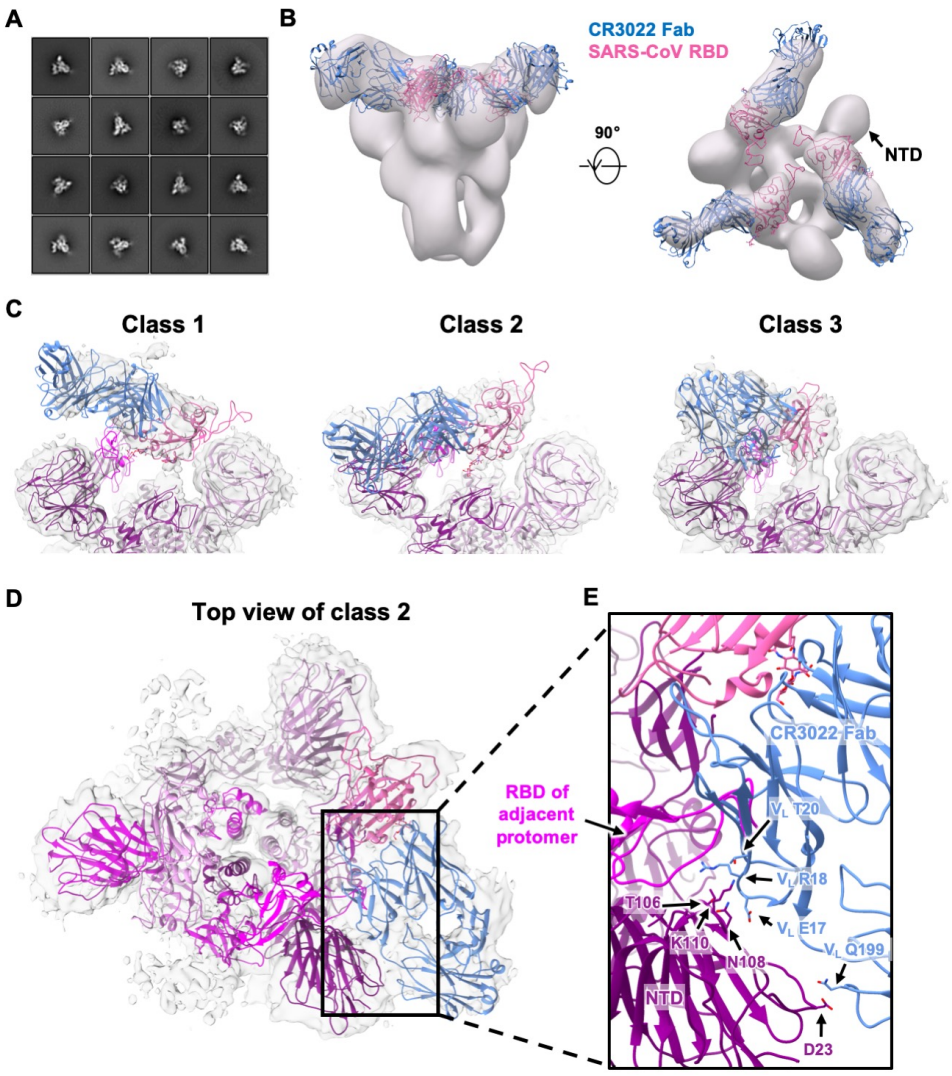

Figure 5. Negative-stain EM and cryo-EM analysis of SARS spike bound to CR3022 Fab. (A) Representative 2D nsEM class averages of the trimeric SARS-CoV spike glycoprotein complexed with three CR3022 Fabs. **(B)** Side and top view of the 3D reconstruction showing CR3022 Fabs bound to all 3 RBDs on the SARS-CoV spike. The SARS-CoV RBD-CR3022 complex from the crystal structure is fitted into the nsEM density with the RBD shown in pink and CR3022 Fab in blue. **(C)** Side views of the B-factor-sharpened cryo-EM maps (transparent gray surface representation) representing three different classes of SARS spike with CR3022 Fab with different RBD-Fab orientations. While four different classes were identified, only three classes are shown here because

712 classes 2 and 4 are very similar (Supplementary Figure 4). The RBD-Fab complex model
713 is fit into the densities with the RBDs shown in pink and CR3022 Fabs represented in blue.
714 The atomic model of the apo SARS-CoV spike (PDB 6ACD) [35] is also fit into density
715 with one RBD removed for clarity. The protomers are colored in purple, magenta and deep
716 magenta. **(D)** Top view of the class 2 cryo-EM map depicting potential quaternary contacts
717 between the RBD-bound Fab and the spike NTD in this conformation. In this RBD-Fab
718 conformation, the Fab would clash with the “down” RBD of the adjacent protomer
719 (magenta) and, therefore, the adjacent RBD can only exist in an “up” conformation. **(E)** A
720 close-up view of the Fab-spike interface showing the superimposition of CR3022 Fab and
721 adjacent RBD. The residues that can contribute to quaternary interactions between
722 CR3022 light chain and the NTD in two of the four classes (2 and 4) are shown.

Supplementary Table 1. X-ray data collection and refinement statistics.

Data collection	
Beamline	SSRL 12-2
Wavelength (Å)	0.97946
Space group	C 1 2 1
Unit cell parameters (Å and °)	a=265.7, b=59.9, c=51.7, β=99.8
Resolution (Å)	50.0–2.70 (2.76–2.70)[a]
Unique reflections	21,547 (2,021)[a]
Redundancy	6.7 (5.5)[a]
Completeness (%)	100.0 (100.0)[a]
$\langle I/\sigma_I \rangle$	14.7 (1.0)[a]
R_{sym}[b] (%)	9.2 (86.1)[a]
R_{pim}[b] (%)	5.4 (54.8)[a]
$CC_{1/2}$[c] (%)	99.4 (74.4)[a]
Refinement statistics	
Resolution (Å)	45.0–2.70
Reflections (work)	21,501
Reflections (test)	1,011
R_{cryst}[d] / R_{free}[e] (%)	22.2 / 27.6
No. of atoms	4,872
Macromolecules	4,795
Glycans	42
Solvent	30
Average *B*-value (Å^2)	80
Macromolecules	80
RBD	104
Fab	70
Glycans	30
Solvent	60
Wilson *B*-value (Å^2)	64
RMSD from ideal geometry	
Bond length (Å)	0.005
Bond angle (°)	1.17
Ramachandran statistics (%)	
Favored	95.6
Outliers	0.16
PDB code	7JN5

[a] Numbers in parentheses refer to the highest resolution shell.

[b] $R_{sym} = \Sigma_{hkl} \Sigma_i | I_{hkl,i} - \langle I_{hkl} \rangle | / \Sigma_{hkl} \Sigma_i I_{hkl,i}$ and $R_{pim} = \Sigma_{hkl} (1/(n-1))^{1/2} \Sigma_i | I_{hkl,i} - \langle I_{hkl} \rangle | / \Sigma_{hkl} \Sigma_i I_{hkl,i}$, where $I_{hkl,i}$ is the scaled intensity of the ith measurement of reflection h, k, l, $\langle I_{hkl} \rangle$ is the average intensity for that reflection, and *n* is the redundancy.

[c] $CC_{1/2}$ = Pearson correlation coefficient between two random half datasets.

[d] $R_{cryst} = \Sigma_{hkl} | F_o - F_c | / \Sigma_{hkl} | F_o | \times 100$, where F_o and F_c are the observed and calculated structure factors, respectively.

[e] R_{free} was calculated as for R_{cryst}, but on a test set comprising 5% of the data excluded from refinement.

723

724 **Supplementary Table 2. Cryo-EM data collection and refinement statistics.**

Map	**SARS-CR3022Fab Class 1**	**SARS-CR3022Fab Class 2**	**SARS-CR3022Fab Class 3**	**SARS-CR3022Fab Class 4**
EMDB	Pending	Pending	Pending	Pending
Data collection				
Microscope	FEI Talos Arctica	FEI Talos Arctica	FEI Talos Arctica	FEI Talos Arctica
Voltage (kV)	200	200	200	200
Detector	Gatan K2 Summit	Gatan K2 Summit	Gatan K2 Summit	Gatan K2 Summit
Recording mode	Counting	Counting	Counting	Counting
Nominal magnification	36,000	36,000	36,000	36,000
Movie micrograph pixelsize (Å)	1.15	1.15	1.15	1.15
Dose rate (e^-/[(camera pixel)*s])	5.6	5.6	5.6	5.6
Number of frames per movie micrograph	47	47	47	47
Frame exposure time (ms)	250	250	250	250
Movie micrograph exposure time (s)	11.7	11.7	11.7	11.7
Total dose (e^-/Å^2)	50	50	50	50
Defocus range (μm)	-0.4 to -1.6	-0.4 to -1.6	-0.4 to -1.6	-0.4 to -1.6
EM data processing				
Number of movie micrographs	2952	2952	2952	2952
Number of molecular projection images in map	17,472	28,821	34,803	31,645
Symmetry	C1	C1	C1	C1
Map resolution (FSC 0.143; Å)	6.83	6.24	6.42	6.15
Map sharpening B-factor (Å^2)	-164.6	-147.4	-120.5	-138.1

725

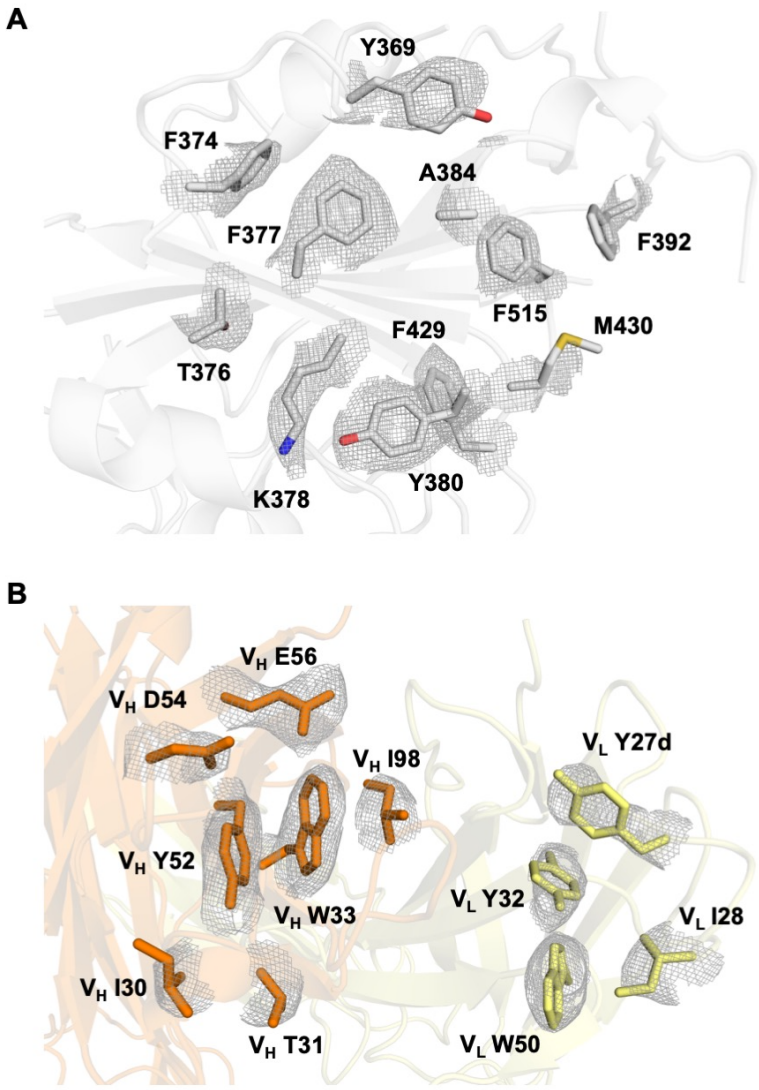

Supplementary Figure 1. X-ray electron density maps for epitope and paratope regions of SARS CoV RBD with Fab CR3022. (A) Final 2Fo-Fc electron density maps for the side chains in the epitope region of SARS-CoV-2 contoured at 1 σ. **(B)** Final 2Fo-Fc electron density maps for the paratope region of CR3022 contoured at 1 σ. The heavy chain is colored in orange, and light chain in yellow. Epitope and paratope residues are labeled.

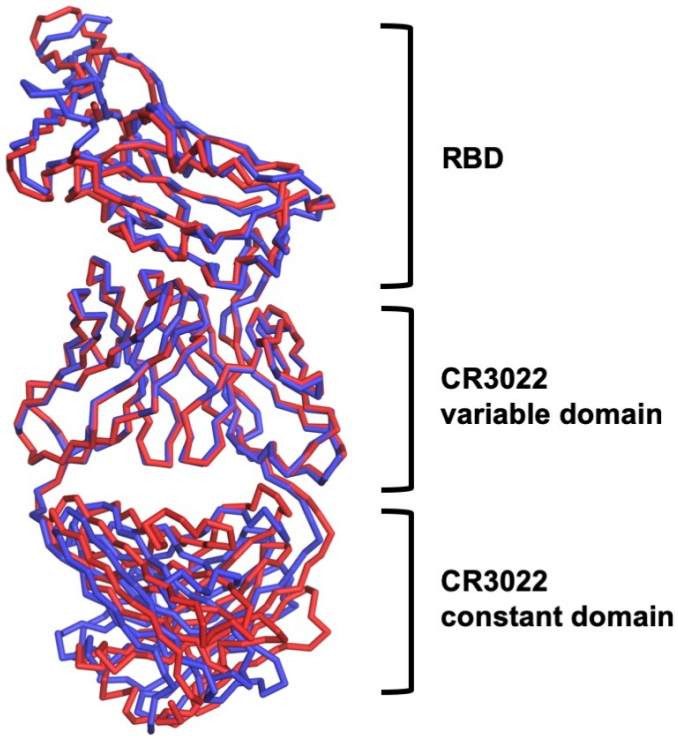

733

734 **Supplementary Figure 2. Structural alignment of CR3022-bound SARS-CoV RBD**
735 **and CR3022-bound SARS-CoV-2 RBD.** Structure of CR3022 in complex with SARS-CoV
736 RBD (this study) is aligned to that with SARS-CoV-2 RBD (PDB 6W41). Structural
737 alignment was performed using CR3022 heavy chain variable domain. Red: CR3022 in
738 complex with SARS-CoV RBD. Blue: CR3022 in complex with SARS-CoV-2 RBD.

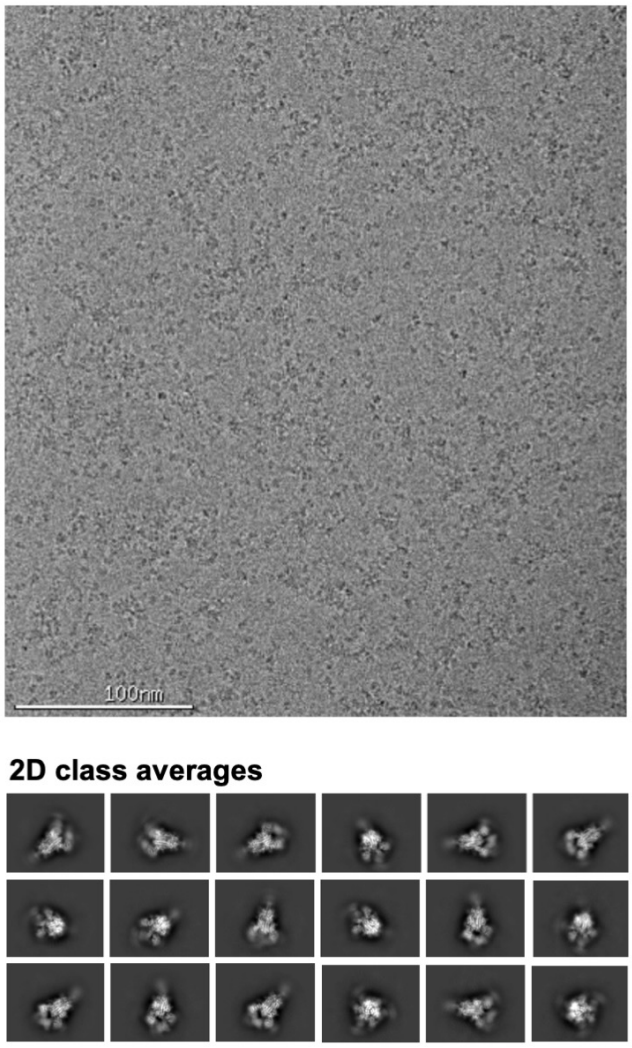

739

740 **Supplementary Figure 3. Representative cryo-electron micrograph and 2D class**
741 **averages of the SARS-CoV spike in complex with CR3022 Fab.** The top panel shows
742 a representative cryo-electron micrograph of the SARS-CoV spike complexed with
743 CR3022 Fab, whereas the bottom panels show the 2D class averages.

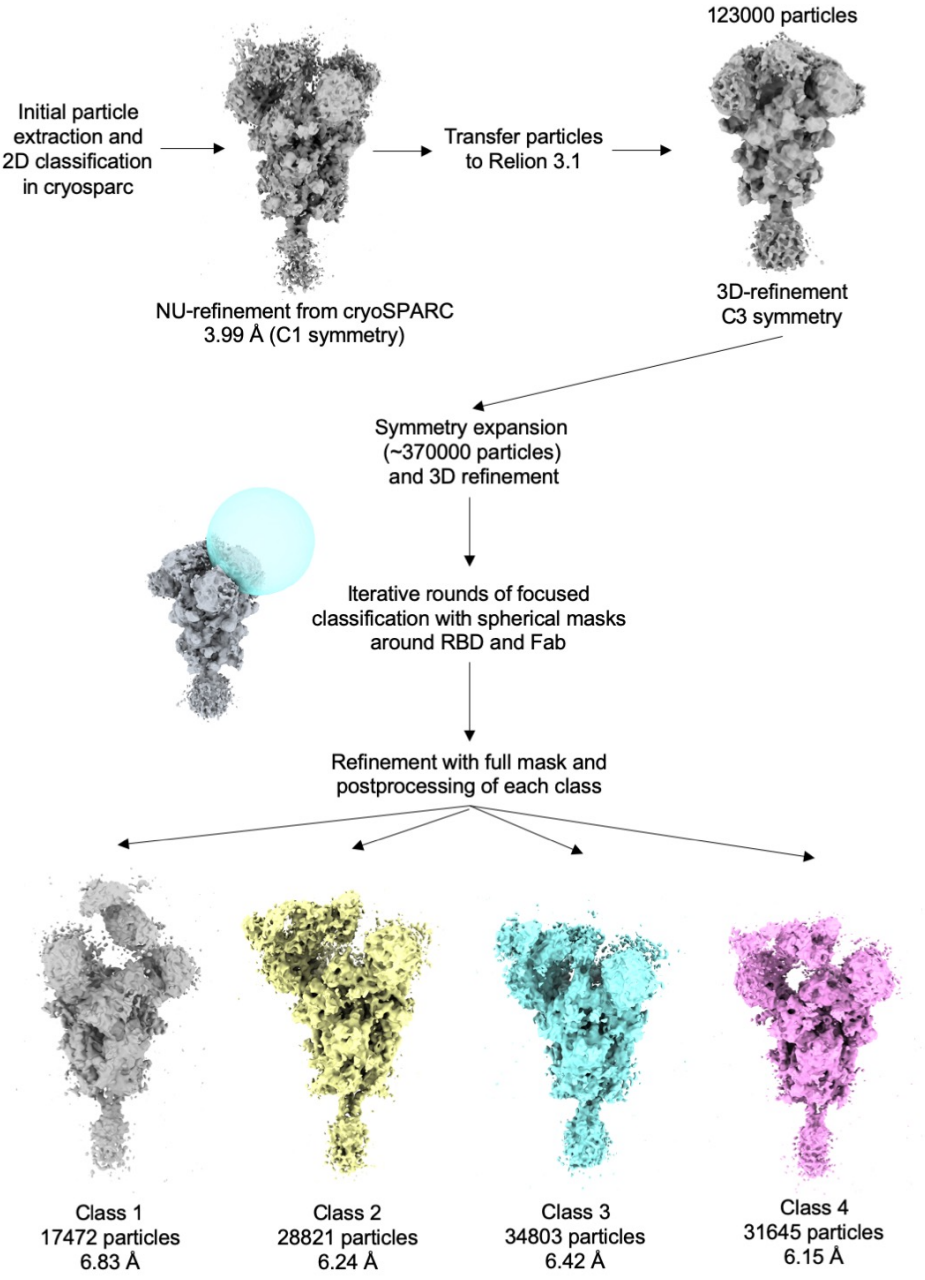

744

745 **Supplementary Figure 4. Workflow for cryo-EM data processing.** Four 3D class
746 averages of complex of the SARS-CoV spike and CR3022 were found during data
747 processing.

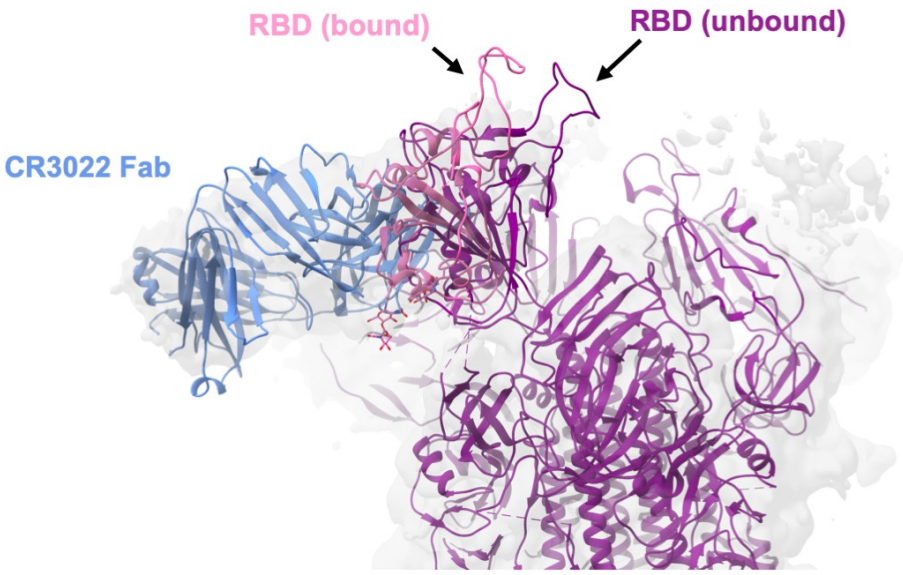

748

749 **Supplementary Figure 5. Comparison of conformations of CR3022-bound and**

750 **unbound RBDs.** The conformation of CR3022-bound RBD in class 2 and 4 is compared

751 to the conformation of RBD on an unliganded SARS-CoV S protein (PDB 6ACD) [35].

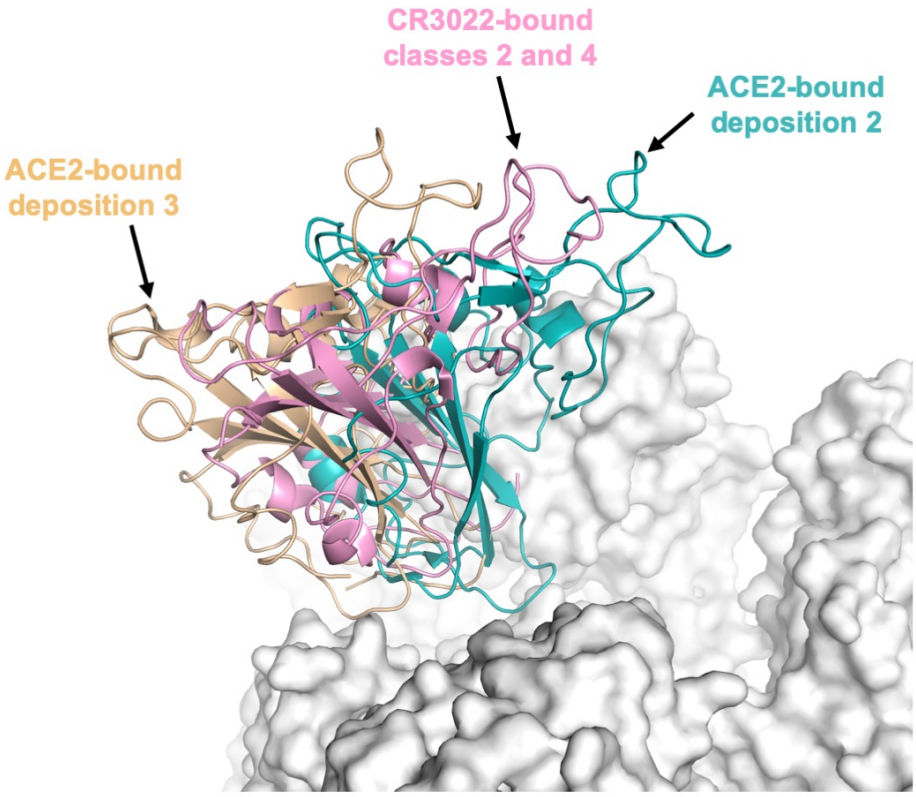

752

753 **Supplementary Figure 6. Comparison of conformations of CR3022-bound and**

754 **ACE2-bound RBDs.** The conformation of CR3022-bound RBD in class 2 and 4 is

755 compared to that of depositions 2 and 3 of ACE2-bound RBD (PDB 6ACJ and 6ACK,

756 respectively) [35].